ANNALS OF GEOPHYSICS, 68, 2, V222, 2025; doi:10.4401/ag-9187
OPEN ACCESS

AI-Powered Mapping of Sundhnúkur's Lava Flows: Sentinel-2 Imagery and Random Forest Modeling for the 2023-2024 Eruption

Arianna Beatrice Malaguti[1]

(1) Istituto Nazionale di Geofisica e Vulcanologia, Sezione di Catania, Osservatorio Etneo, Catania, Italy

Article history: received October 18, 2024; accepted March 14, 2025

Abstract

Volcanic thermal anomalies are commonly monitored using advanced optical satellite sensors, enhancing the detection of renewed volcanic activity. Traditionally, fixed-threshold hotspot detection algorithms have been widely applied to identify these anomalies, effectively minimizing false alarms. However, the mapping of lava flows and monitoring of volcanic activity, which is essential for hazard mitigation and understanding the behavior of active volcanoes, has been further improved through the use of Machine Learning techniques. These methods allow for the rapid processing of large datasets, making them especially valuable for volcanic studies. Here, a Machine Learning approach based on a Random Forest algorithm, designed and implemented on Google Earth Engine, using data from the Sentinel-2 multispectral sensor (S2-MSI), is applied to detect and accurately map lava flows from the 2023-2024 eruption in Sundhnúkur, Iceland. Despite gaps in satellite coverage due to technical issues or adverse weather, the flow maps generated by the algorithm closely align with the actual lava flow fields. The results demonstrate that the Random Forest model, despite not being trained on this study area, exhibits strong generalization capabilities and high sensitivity to subtle volcanic thermal anomalies.

Keywords: Sundhnúkur eruptions; Reykjanes peninsula; Machine Learning; Random Forest; Google Earth Engine; Sentinel 2 – MSI

1. Introduction

Lava flows are one of the most visually striking and destructive phenomena produced by volcanic eruptions. They are formed when molten or partially molten rock is expelled from the Earth's crust and spread over the surface, influenced by the complex interplay of thermal, rheological, and dynamic factors (Griffiths, 2000; Gregg, 2017). This interaction dictates the flow's characteristics, such as its structure, velocity, and the nature of any instabilities within the flow front. The behavior of lava flows is primarily determined by the properties of the erupted magma – its viscosity, gas content, and temperature – as well as the effusion rate and the topography of the area the lava traverses (Griffiths, 2000; Diniega et al., 2013; Gregg, 2017). These flows range from the slow-moving, viscous lava characteristic of subduction zones to the more fluid basaltic flows typical of volcanic hotspots.

Basaltic lava flows are generally dominant in volcanic 'hotspots' such as Hawaii and Iceland, where low-viscosity lava can travel great distances from the eruption site, producing extensive flow fields (Soule, 2015; Cas et al., 2024). These regions are typified by effusive eruptions that produce lava fountains, flows, and spatter cones. In contrast, volcanoes situated in active subduction zones – such as those in western North America, Indonesia, Philippines, and Japan – tend to produce lava with much higher apparent viscosity and lower temperatures (Manea and Gurnis, 2007; Horiuchi and Iwamori, 2016). The higher viscosity of these lavas often results in the formation of lava domes, which can collapse to generate block-and-ash flows or, in some cases, lead to explosive pyroclastic flows, as seen in volcanoes like Soufrière Hills, Monserrat (Calder et al., 2002).

The destructive power of lava flows is well documented, with recent events like the Cumbre Vieja eruption in La Palma (2021) underscoring their ability to devastate everything in their path-whether by burning, burying, or incinerating structures and landscapes (Carracedo et al., 2022). The hazards increase exponentially when lava interacts with other elements of the environment, such as ice or snow, which can trigger far-reaching lahars, as was the case with the Eyjafjallajökull eruption in Iceland in 2010 (Gudmundsson et al., 2012). Given their significant impact on human settlements and infrastructure, the ability to accurately map and monitor lava flows in near real-time is essential for hazard mitigation and risk assessment.

Traditionally, lava flows have been mapped directly in the field, using methods like ground-based surveys or observations from Unmanned Aerial Vehicles (UAVs) (Frazzetta and Romano, 1984; Calvari et al., 1994; Spampinato et al., 2011; Del Negro et al., 2016). While effective in certain contexts, these methods are limited by the size of flow fields, overlap with previous flows, the presence of dense vegetation, and the general inaccessibility of volcanic areas during active eruptions. Consequently, remote sensing techniques have become increasingly common for comprehensive analysis of lava flow fields, offering critical insights that are impossible to obtain through traditional methods alone (Abrams et al., 1991; Kervyn et al., 2007; Blackett, 2013; Del Negro et al., 2016; Corradino et al., 2019, 2022).

One common remote sensing technique is the comparison of pre- and post-eruptive Digital Elevation Models (DEMs), which can help identify changes in topography caused by the emplacement of lava (Albino et al., 2015; Ganci et al., 2019). However, the efficacy of this approach is often limited by the availability of detailed pre-eruptive topography, especially in cases where frequent eruptions occur, or the volcano is poorly monitored. Even where DEMs are available, rapid changes in lava flow fields can render this approach inadequate during ongoing effusive crises.

To address these limitations, satellite-based remote sensing offers a powerful alternative for near real-time monitoring. Modern space-based sensors capture multispectral data that provide valuable information about the thermal, structural, and compositional characteristics of lava flows. For instance, the electromagnetic energy emitted or reflected by lava flows can be measured in the visible (VIS), near-infrared (NIR), short-wave infrared (SWIR), mid-infrared (MIR), and thermal infrared (TIR) wavelengths, all of which provide distinct signatures for discriminating fresh lava from older or cooler surfaces (Harris, 2013). Normalized Hotspot Indices (NHI), which leverage the SWIR and NIR bands, have been widely employed to monitor volcanic activity and have proven effective in tracking eruptive events globally (Marchese et al., 2019, 2021).

In addition to optical remote sensing, radar satellite data, particularly synthetic aperture radar (SAR), play an important role in detecting volcanic activity. SAR-based coherence analysis, which compares images captured at different times, can detect low-coherence areas associated with lava flow emplacement (Lu et al., 2004; Dietterich et al., 2012; Ferrentino et al., 2023). SAR's ability to operate under any weather condition (e.g., cloud cover), under vegetation cover and at night makes it invaluable for continuous monitoring (Ferrentino et al., 2023). A constellation of SAR satellites can collect images of the same region more frequently than the average weekly repetition time for ground-based mapping. Finally, non-lava sources have also been mapped with SAR coherence, such as pyroclastic flows from Soufrière Hills volcano, Montserrat (Wadge et al., 2002), and the Portuguese Bend landslide in California (Calabro et al., 2010). However, the use of SAR images has some limitations, such as the uncertainty in interpreting decorrelated regions and the persistence of decorrelation, which can obscure new activity (Dietterich et al., 2012). Combining SAR with optical and infrared data can improve accuracy and overcome some of these challenges (Lu et al., 2004).

In recent years, the integration of Machine Learning (ML) techniques with satellite data has further revolutionized volcanic hazard monitoring (Amato et al., 2023; Cariello et al., 2023; Corradino et al., 2024; Torrisi et al., 2024). Advances in cloud computing and open-source platforms, such as Google Earth Engine (GEE), have made it feasible to analyze decades-long time series of satellite images over vast regions (Gorelick et al., 2017; Hird et al., 2017). GEE provides access to massive archives of multispectral data and offers the computational power necessary to process

and analyze these datasets efficiently. Machine Learning algorithms, particularly the Random Forest model, have emerged as effective tools for classifying complex features and predicting volcanic hazards based on multispectral inputs (Corradino et al., 2022; Amato et al., 2021; Cariello et al., 2023).

The combination of remote sensing data with Machine Learning techniques has enabled the semi-automatic mapping of lava flows, significantly reducing the time and labor required for manual mapping (Servadio et al., 2012; Kubanek et al., 2015; Marchese et al., 2019). For example, data-driven approaches, such as those developed by Corradino et al. (2022), have demonstrated the ability to detect and map thermal anomalies associated with lava flows quickly and with high precision. These advances are crucial for near real-time hazard monitoring, particularly in areas where rapid and unpredictable volcanic events pose significant risks.

Here, I applied the Corradino et al. (2022)'s Random Forest algorithm within Google Earth Engine to map lava flows from the Sundhnúkur eruption in Iceland, which occurred from December 2023 to September 2024. Using multispectral data from the Sentinel-2 satellite's Multispectral Imager (MSI), I aimed to accurately detect and map the spatial extent of lava flows, by passing the need for fixed-threshold hotspot detection methods and providing a more flexible and data-driven approach.

2. Geological background

Iceland is a unique geological environment located at the intersection of the North American and Eurasian plates. This hotspot, situated on the Mid-Atlantic Ridge, is marked by a combination of rifting and volcanic activity, with the plate boundary in the NE-Atlantic characterized by rift and transform segments. These segments generally form well-defined plate boundaries but become increasingly complex as they cross Iceland, due to the interaction between the tectonic plates and the underlying mantle plume (Wolfe et al., 1997). Within Iceland, the boundary between the plates branches into oblique rift segments and tectonic blocks that move independently, forming complex systems of volcanic activity and faulting. This complexity is exemplified by the Reykjanes Peninsula Rift (RPR) in the southwest and the Grímsey Oblique Rift (GOR) in the north, where divergent and transform tectonism occurs in tandem.

The Reykjanes Peninsula, as part of the Reykjanes Ridge, is structurally significant, having undergone several rifting episodes over the last 4000 years (Einarsoon, 2008; Sæmundsson et al., 2020). These episodes activated the peninsula's volcanic systems, leading to significant basaltic eruptions every 800-1000 years. The volcanic systems on the peninsula – Reykjanes, Svartsengi, Krýsuvík, and Brennisteinsfjöll – have produced notable eruptions throughout history, with the most recent rifting cycle initiating a series of eruptions in the Fagradalsfjall area in 2021, 2022, and 2023 (Sæmundsson and Sigurgeirsson, 2013). The most recent eruption cycle marked a return to activity in the Reykjanes Volcanic Belt after nearly 800 years of dormancy (Bindeman et al., 2022; Fig. 1).

In the northeast of the Reykjanes Peninsula lies the Sundhnúkur volcanic system, which has emerged as a key site of interest in recent years. Sundhnúkur, part of the Svartsengi Volcanic Lineament, is located near the town of Grindavík and has a history of effusive basaltic eruptions typical of Iceland's volcanic systems. The 2023-2024 eruption of Sundhnúkur has been a focal point for scientists, as it is one of the most significant volcanic events in the region in recent times. This eruption followed a major tectonic event in the area and resulted in multiple lava flows, significantly altering the landscape.

The Sundhnúkur volcanic system reawakened in December 2023, after several decades of quiescence. The eruption cycle was characterized by multiple effusive events, with lava flows occurring in December 2023, January and February 2024, and more prolonged activity from March to May 2024. Another eruption followed in late May and continued until June, with a final event beginning in August and ending in September 2024. These eruptions have been characterized by relatively low-viscosity basaltic lava flows, similar to other volcanic systems in Iceland (Iceland Meteorological Office – IMO, 2024 – https://en.vedur.is/about-imo/news/; Fig. 1).

The 2023-2024 eruption produced extensive lava fields and significantly impacted the surrounding region. Sundhnúkur's location near key infrastructure, including the town of Grindavík, raised concerns about the potential hazards posed by lava flows, volcanic gases, and ashfall. The lava flows themselves, composed of basaltic magma, exhibited behavior typical of Icelandic volcanism, with rapid effusion rates and the formation of broad, low-lying flow fields (Caracciolo et al., 2024). These flows were monitored closely using advanced satellite remote sensing techniques, which provided near real-time data on the extent and progression of the lava.

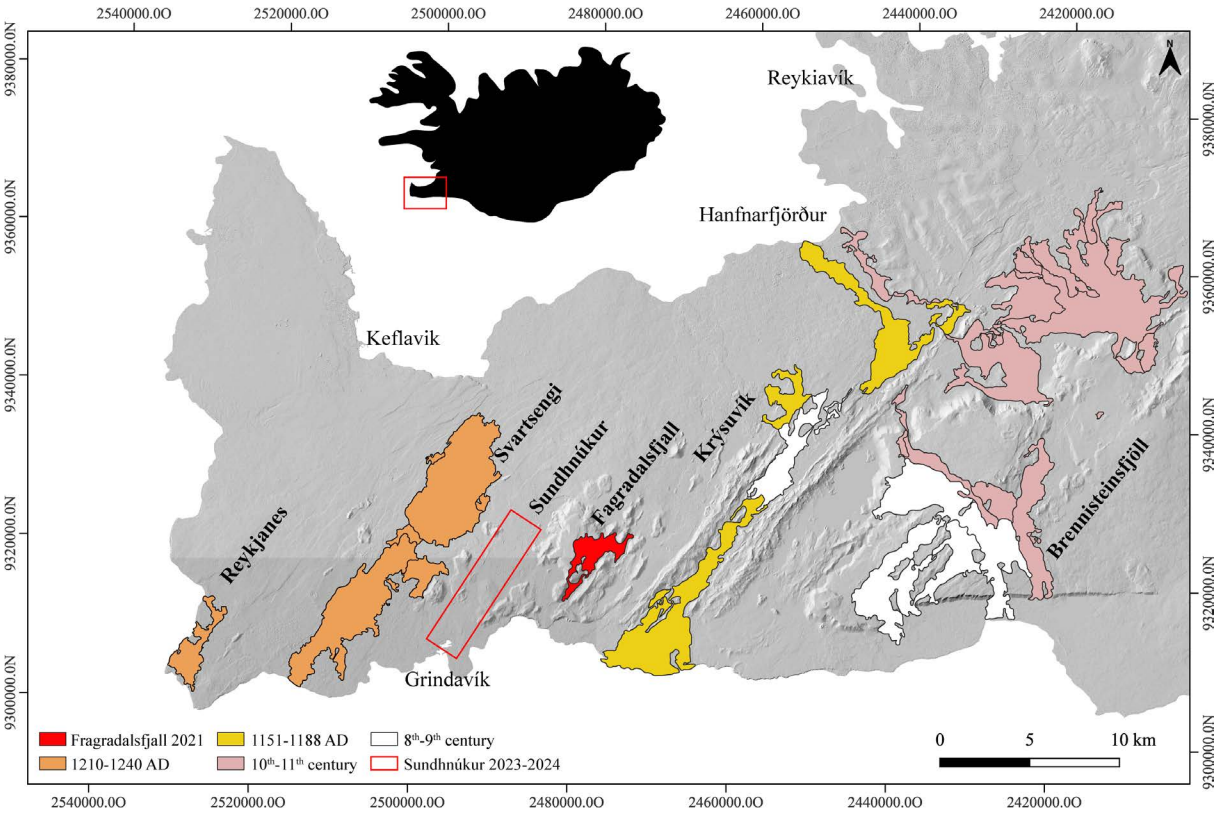

Figure 1. Geological setting of Reykjanes Peninsula lava flows emplaced in the Reykjanes, Svartsengi, Fagradalsjall, Krýsuvík and Brennisteinsfjöll volcanic systems from 8th century to 2021. The 2023-2024 AD Sundhnúkur eruptions area is also illustrated (IMO, 2024). Geological data are from Iceland GeoSurvey (ÍSOR) (Sæmundsson et al., 2016). Coordinates are in decimal degrees using the WGS84 reference system.

3. Satellite Data

Sentinel-2 is a satellite constellation operated by the European Space Agency (ESA) as part of the Copernicus program, designed for high-resolution, multispectral Earth observation. The constellation consists of two identical sun-synchronous satellites, Sentinel-2A and Sentinel-2B, which work together to provide global monitoring capabilities. With a revisit period of 10 days per satellite, the constellation achieves a combined global coverage of every 5 days. This high temporal resolution is essential for dynamic environmental monitoring, including tracking volcanic activity.

Each satellite is equipped with a state-of-the-art Multi-Spectral Instrument (MSI) capable of capturing imagery across 13 spectral bands. These bands span the visible (VIS), near-infrared (NIR), red-edge, and short-wave infrared (SWIR) portions of the electromagnetic spectrum. The MSI provides data at varying spatial resolutions, including 10 meters for the visible and near-infrared bands, 20 meters for the red-edge and SWIR bands, and 60 meters for atmospheric correction bands. This range of resolutions makes Sentinel-2 particularly well-suited for detecting and analyzing volcanic phenomena such as lava flows, and surface temperature changes.

Sentinel-2 data are processed and provided at different product levels, most notably Level-1C and Level-2A (Gorelick et al., 2017). Level-1C products consist of orthorectified Top-Of-Atmosphere (TOA) reflectance measurements, while Level-2A products are atmospherically corrected surface reflectance (SR) data. Both levels are available through Google Earth Engine (GEE), where the data can be processed and analyzed for volcanic hazard monitoring.

TOA reflectance values were converted to radiance units (W m^{-2} sr^{-1} μm^{-1}) to facilitate precise analysis. Specifically, radiance measurements from seven Sentinel-2 spectral bands were utilized: B2 (492.1 nm for S2B, 496.6 nm for S2A), B3 (559 nm for S2B, 560 nm for S2A), B4 (665 nm for S2B, 664.5 nm for S2A), B5 (703.8 nm for S2B, 703.9 nm for S2A), B8A (864 nm for S2B, 864.8 nm for S2A), B11 (1610.4 nm for S2B, 1613.7 nm for S2A), and B12 (2185.7 nm for S2B, 2202.4 nm for S2A). These bands, referred to as $L_{0.4}$, $L_{0.5}$, $L_{0.6}$, $L_{0.7}$, $L_{0.8}$, $L_{1.6}$, and $L_{2.2}$, respectively, were critical for analyzing the spectral properties of the lava flows and other volcanic features during the 2023-2024 Sundhnúkur eruption.

4. Method

The methodology employed in this study is based on a supervised ML algorithm developed within Google Earth Engine (GEE) by Corradino et al. (2022). This algorithm utilizes spectral data from Sentinel-2's Multi-Spectral Instrument (S2-MSI) to accurately identify and discriminate thermal anomalies (class 1) from background elements such as snow and clouds (class 0). The outlines of the anomaly are shown in yellow and the hottest pixels within the segmented anomaly in red. The result of the spectral responses of each pixel is analyzed considering that the red color indicates the use of bands in the spectrum that allow only very hot bodies to be visualized, while yellow refers to bands that are also sensitive to lower temperatures, allowing for the detection of cooling bodies. By leveraging the distinct spectral characteristics of these features, the algorithm achieves high performance in detecting volcanic thermal anomalies.

Feature Selection

In Corradino et al. (2022), two ML models are trained using two sets of spectral features, Feat1 and Feat2 (Table 1), which are designed to enable effective discrimination between thermal anomalies and background elements.

– Feat1: This set is based on a set of bands already used to successfully recognize anomalies worldwide, minimizing false alarms (Table 1; Genzano et al., 2020). In particular, it focuses on Normalized Hotspot Index (NHI), which is well-suited for identifying mid-intensity thermal anomalies. These indices primarily use bands from the near-infrared (NIR) and shortwave infrared (SWIR) regions of the spectrum, which are sensitive to high-temperature thermal activity. This set minimizes false positives by concentrating on strong thermal variations. For volcanic monitoring, three key normalized indices are employed (Eq. (1), (2) and (3); Genzano et al., 2020; Marchese et al., 2019):

  - $\mathrm{NHI_{SWNIR}} = \frac{L_{1.6} - L_{0.8}}{L_{1.6} + L_{0.8}}$; a normalized hotspot index derived from SWIR1 and NIR bands. (1)

  - $\mathrm{NHI_{SWIR}} = \frac{L_{2.2} - L_{1.6}}{L_{2.2} + L_{1.6}}$; an index based on SWIR2 and SWIR1 bands. (2)

  - ND (Normalized Difference Index) $= \frac{L_{2.2} - L_{0.8}}{L_{2.2} + L_{0.8}}$; a normalized index that combines SWIR2 and NIR bands. (3)

  These indices are particularly effective in isolating areas with significant thermal activity, reducing the likelihood of false alarms caused by non-thermal features.

– Feat2: To enhance the model's ability to detect less intense thermal anomalies, Feat2 includes additional spectral bands from visible (VIS) to SWIR (Table 1). This set helps the algorithm learn the spectral signatures of diverse background elements such as snow, clouds, and vegetation, improving the model's sensitivity to subtle thermal variations (Spinetti et al., 2009; Corradino et al., 2019).

Feat1	Feat2
$L_{0.7}$	$L_{0.4}$
$L_{1.6}$	$L_{0.5}$
$L_{2.2}$	$L_{0.6}$
ND	$L_{0.8}$
$\mathrm{NHI_{SWNIR}}$	$L_{1.6}$
$\mathrm{NHI_{SWIR}}$	$L_{2.2}$

Table 1. Feature sets used for the two models, namely Feat1 and Feat2, from Corradino et al. (2022).

Data Preprocessing and Model Training

In Corradino et al. (2022), input data for each eruptive event consists of a total of 10 Sentinel-2 MSI images from volcanoes such as Etna, Geldingadalir, Cumbre Vieja, Stromboli and Pacaya, which are normalized using z-score normalization. This normalization technique ensures that the data are standardized, allowing the model to perform effectively across different spectral ranges. The target consists in a binary image in which pixels with value 1 represent thermal anomalies and those with value 0 correspond to the background. Target images were obtained from high spatial resolution data from the S2-MSI sensor, with the positions of hot pixels manually determined by experts through visual inspection (Lu et al., 2004). As a result, the target maps have a spatial resolution of 20 m, corresponding to the band with the lowest resolution. Because minor thermal anomalies are the most difficult to detect, pixels with lower temperatures were included in the training images, with the B12 band having a minimum radiance value of 0.68 ($W\ m^{-2}\ sr^{-1}\ \mu m^{-1}$).

The classification process in Corradino et al. (2022) is based on the Random Forest (RF) algorithm, which is known for its robustness and ability to handle complex datasets while minimizing overfitting (Hastie et al., 2009). The RF algorithm uses an ensemble of decision trees to improve classification accuracy through bagging, which aggregates multiple decision trees to reduce variance and increase generalization.

Two Random Forest models are trained:

- RF1 is trained with Feat1, which emphasizes the use of NIR and SWIR bands for detecting medium to high-intensity thermal anomalies.
- RF2 incorporates Feat2, which includes visible bands in addition to SWIR and NIR, enhancing the model's sensitivity to weak or subtle thermal anomalies by capturing finer spectral distinctions in the background environment.

These models use 100 decision trees, a number selected to balance classification performance and computational efficiency (Ghimire et al., 2012). This configuration proved effective in optimizing both accuracy and speed of classification without overfitting to the training data (Corradino et al., 2022).

Model Evaluation

After training, the model is evaluated by Corradino et al. (2022) using standard performance metrics, including accuracy, precision, and recall (Bilotta et al., 2019; Corradino et al., 2019). These metrics assess how well the model's predictions align with the actual locations of thermal anomalies. Precision measures the proportion of correctly identified thermal anomalies, while recall indicates the model's ability to detect all true positives.

Corradino et al. (2022)'s results showed that the Random Forest approach outperformed traditional fixed-threshold algorithms, particularly in detecting less intense thermal anomalies. The RF2 model, which incorporated visible bands, demonstrated superior performance by capturing subtle thermal variations that might have been missed by algorithms relying solely on infrared bands. This model also showed a reduction in false negatives, making it a valuable tool for early detection of weak volcanic thermal activity (Corradino et al., 2022).

5. Results

The combination of the high spatial, temporal, and spectral resolution provided by Sentinel-2 enabled a detailed analysis of the Sundhnúkur eruption, offering valuable insights into the progression of lava flows, surface composition changes, and the identification of volcanic hotspots. By utilizing the multi-temporal capabilities of Sentinel-2 data and Machine Learning techniques, particularly the Random Forest model RF2 developed in Google Earth Engine by Corradino et al. (2022), I successfully tracked and mapped the lava flows produced during 2023-2024 eruptions.

5.1 18-21 December 2023

On the night of December 18, 2023, a volcanic eruption began north of Grindavík on the Reykjanes Peninsula, ending on December 21. The eruption occurred near Sundhnúkagígar, approximately four kilometers northeast of Grindavík (Fig. 1; IMO, 2024). Unfortunately, no S2-MSI satellite images were available between November 13, 2023, and January 17, 2024 (EO Browser). The reconstruction of the lava field was achieved using data from IMO (2024) and Willsey and Günzler (2024) (Fig. 2).

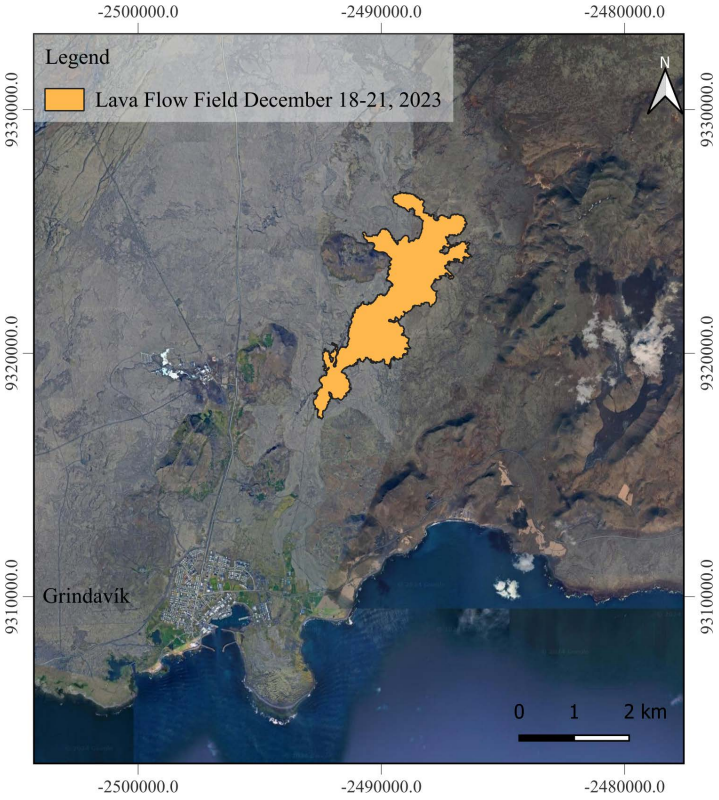

Figure 2. Map of the lava flow field of December 18-21, 2023. Geological data are from Willsey and Günzler (2024) and IMO (2024). Coordinates are in decimal degrees using the WGS84 reference system.

5.2 14-16 January 2024

A new eruption began on the morning of January 14, 2024, with a fracture opening about 900 meters from the town of Grindavík (IMO, 2024). Once again, no S2-MSI images were available until January 17. However, as shown in Fig. 3a, the Random Forest algorithm by Corradino et al. (2022) successfully identified thermal anomalies associated with the cooling lava field during this period. Figure 3b shows the December 2023 and January 2024 lava field mapping obtained from Willsey and Günzler (2024) and IMO (2024) geological data. It can be seen that the thermal anomaly detected in Fig. 3a corresponds to the cooling lava field of January 2024.

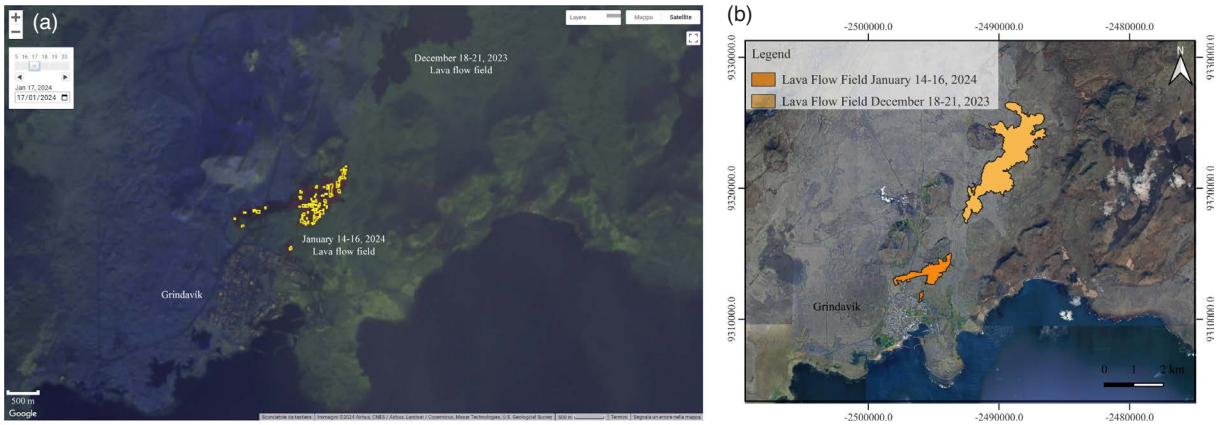

Figure 3. (a) Thermal anomaly map from S2-MSI of 17 January 2024 near the town of Grindavík. The cooling lava field can be observed. All the images were captured via Google Earth Engine. The figure shows the contours of the anomaly in yellow and the hottest pixels within the segmented anomaly in red. (b) Map of the lava flow fields of December 18-21, 2023, and January 14-16, 2024. Geological data are from Willsey and Günzler (2024) and IMO (2024). Coordinates are in decimal degrees using the WGS84 reference system.

5.3 08-09 February 2024

On February 8, 2024, another eruption occurred at a location close to that of December 18, 2023, which ended the next day (IMO, 2024). Figure 4 shows the thermal anomalies for the active lava field on February 8 (Fig. 4a) and for the cooling lava field on February 11, 2024 (Fig. 4b). An excellent correspondence can be observed between the detected thermal anomaly (Fig. 4a) and the lava field map obtained from the geological data of Willsey and Günzler (2024) and IMO (2024).

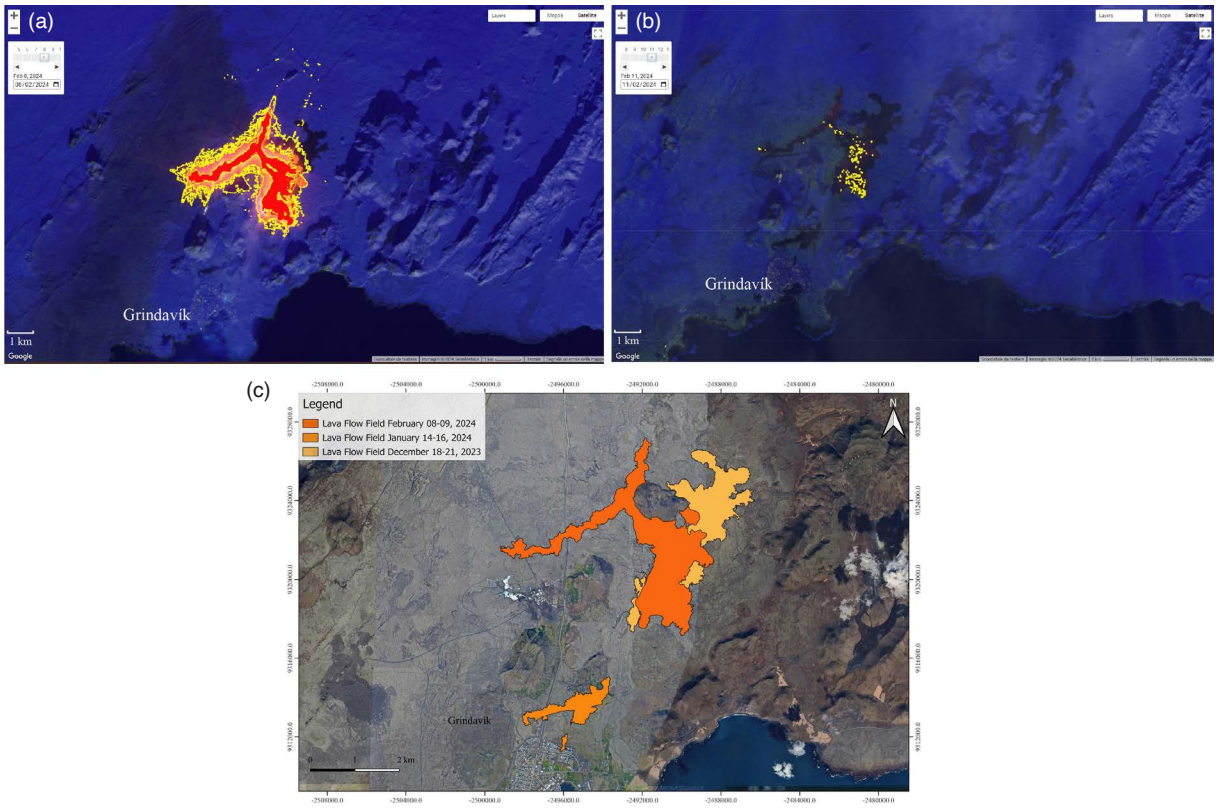

Figure 4. Thermal anomaly map from S2-MSI of (a) 08 February 2024 and (b) 11 February 2024, near the town of Grindavík. All the images were captured via Google Earth Engine. The figure shows the contours of the anomaly in yellow and the hottest pixels within the segmented anomaly in red. (c) Map of the lava flow fields of December 18-21, 2023, January 14-16, 2024, and February 08-09, 2024. Geological data are from Willsey and Günzler (2024) and IMO (2024). Coordinates are in decimal degrees using the WGS84 reference system.

5.4 16 March – 08 May 2024

A month after the last event, a new eruption began on March 16, 2024, marked by the rapid formation of a 2.9-kilometer-long fissure, similar in length and position to that of the February 8, 2024 eruption (IMO, 2024). Due to persistent cloud cover, the first available S2-MSI image was taken on March 29, 2024 (Fig. 5a). From April 5 onward, S2-MSI images confirm only one active vent (Figs. 5c-e). According to the IMO, on April 27, lava from the crater reached the eastern defense wall of Grindavík, eventually crossing it (Fig. 5f; IMO, 2024). This is corroborated by S2-MSI satellite images, which identify a thermal anomaly near Grindavík (Fig. 5f). The last cloud-free image was captured on April 26, 2024 (Fig. 5f), and the eruption was declared over on May 8. It is possible to observe that the algorithm succeeds well in identifying only the hottest thermal anomalies (Figs. 5a-b-c-d-e-f), such as the vent and lava flows closest to the effusive mouths, while it has difficulty in recognizing the entire advance of the lava field due to the rapid cooling of the upper part of the lava flow. Figure 5a shows false positives in the cloud west of Grindavík. Figure 5g shows the lava flow fields map of December 18-21, 2023, January 14-16, 2024, February 08-09, 2024, and March 16-May 8, 2024 (geological data from Willsey and Günzler, 2024 and IMO, 2024).

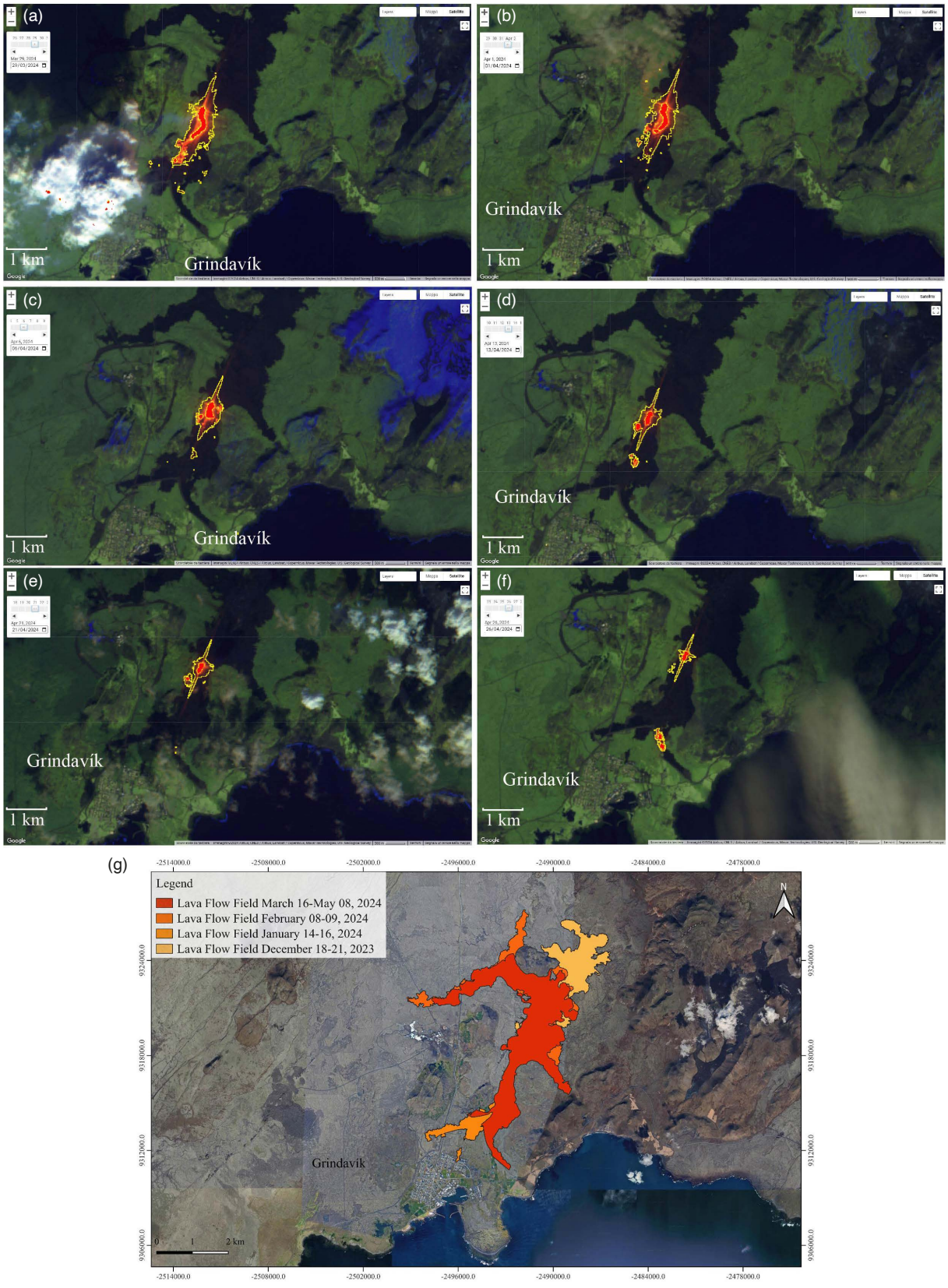

Figure 5. Thermal anomaly map from S2-MSI of (a) 29 March 2024; (b) 01 April 2024; (c) 06 April 2024; (d) 13 April 2024; (e) 21 April 2024; (f) 26 April 2024, near the town of Grindavík. All the images were captured via Google Earth Engine. The figure shows the contours of the anomaly in yellow and the hottest pixels within the segmented anomaly in red. g) Map of the lava flow fields of December 18-21, 2023, January 14-16, 2024, February 08-09, 2024, and March 16-May 08, 2024. Geological data are from Willsey and Günzler (2024) and IMO (2024). Coordinates are in decimal degrees using the WGS84 reference system.

5.5 29 May – 24 June 2024

On May 29, 2024, another eruption occurred along the road to Grindavík, a few kilometers from the village (IMO, 2024). The first S2-MSI image was taken on June 2, 2024 (Fig. 6a). The IMO reported a single active crater from June 4, which was confirmed by the S2-MSI images and the Random Forest algorithm (Figs. 6b-e). The eruption ended on June 24, 2024 (IMO, 2024). In the following days, satellite images and the Random Forest algorithm identified thermal anomalies consistent with cooling lava fields (Fig. 6f). Figure 6g shows the lava flow field map of December 18-21, 2023, January 14-16, 2024, February 08-09, 2024, March 16-May 8, 2024, and May 29-June 24, 2024. Geological data are taken from Willsey and Günzler (2024) and IMO (2024).

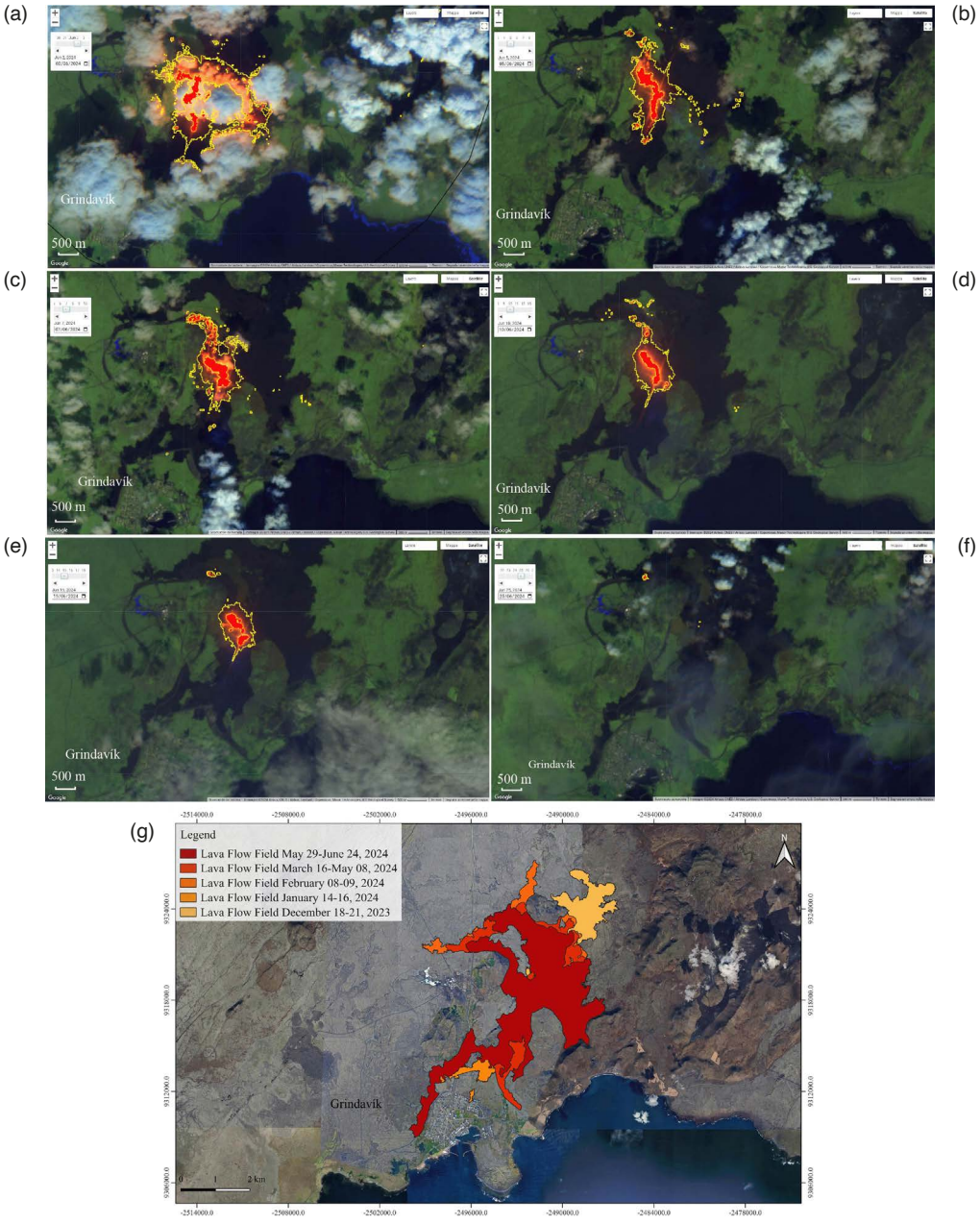

Figure 6. Thermal anomaly map from S2-MSI of (a) 02 June 2024; (b) 05 June 2024; (c) 07 June; (d) 10 June 2024; (e) 15 June 2024; (f) 25 June 2024, near the town of Grindavík. All the images were captured via Google Earth Engine. The figure shows the contours of the anomaly in yellow and the hottest pixels within the segmented anomaly in red. (g) Map of the lava flow fields of December 18-21, 2023, January 14-16, 2024, February 08-09, 2024, March 16-May 08, 2024, and May 29-June 24, 2024. Geological data are from Willsey and Günzler (2024) and IMO (2024). Coordinates are in decimal degrees using the WGS84 reference system.

5.6 22 August – 06 September 2024

After nearly two months of quiescence, a new eruptive phase began on August 22, 2024, with the opening of a fissure east of Sýlingarfell, initially extending both north and south (IMO, 2024). Due to persistent cloud cover, only four S2-MSI satellite images were available during this time (Figs. 7b-c). Figure 7d depicts the cooling phase of the new lava field. Notably, Fig. 7a shows a thermal anomaly detected by the Random Forest algorithm three days before the eruption, along the fracture that later produced the August-September lava field. The eruption officially ended on September 06, 2024. Complete mapping of the lava field was obtained from geological data of Willsey and Günzler (2024) and IMO (2024) (Fig. 7e).

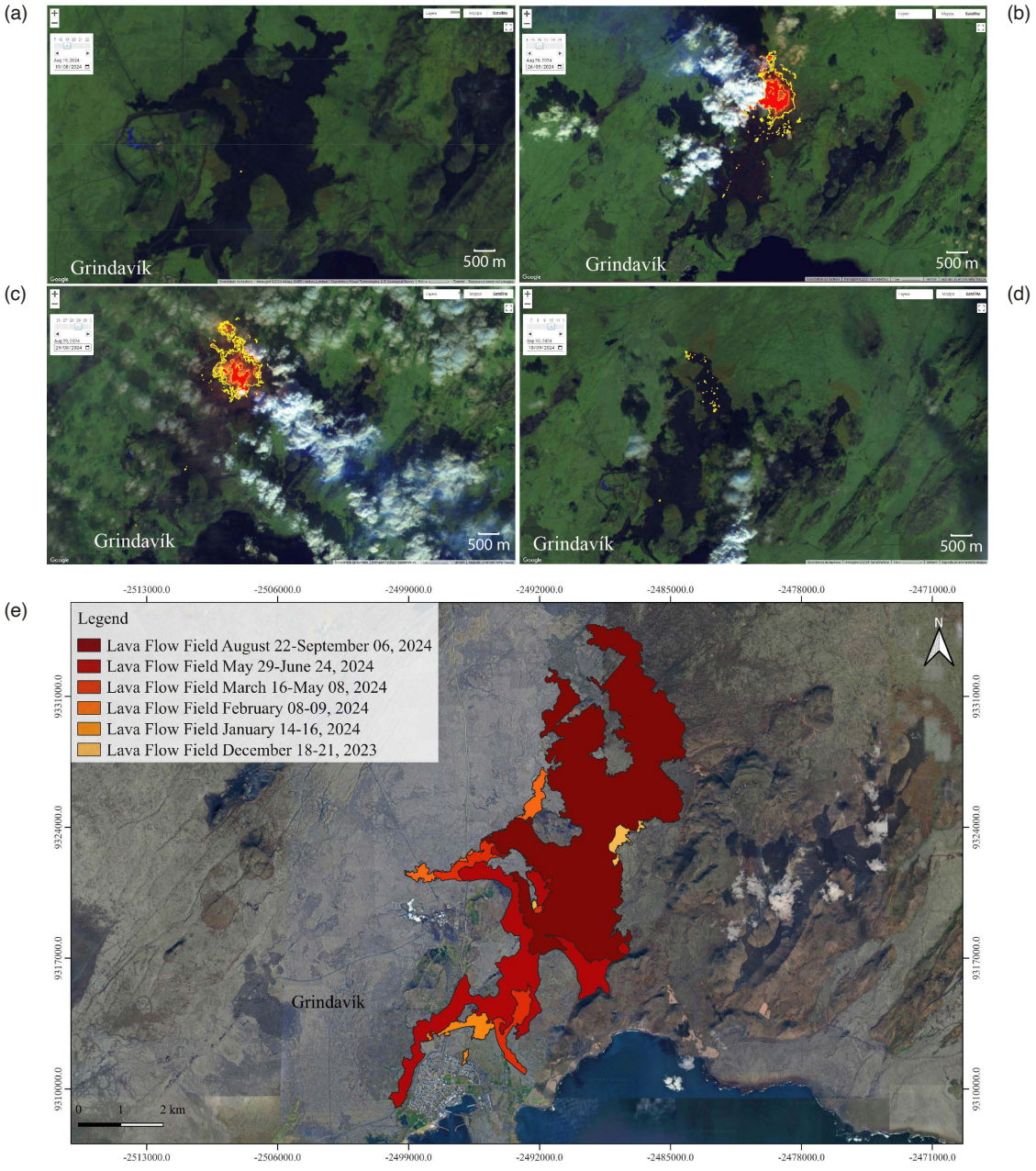

Figure 7. Thermal anomaly map from S2-MSI of: (a) 19 August 2024; (b) 26 August 2024; (c) 29 August 2024; (d) 10 September 2024, near the town of Grindavík. All the images were captured via Google Earth Engine. The figure shows the contours of the anomaly in yellow and the hottest pixels within the segmented anomaly in red. (e) Map of the lava flow fields of December 18-21, 2023, January 14-16, 2024, February 08-09, 2024, March 16-May 08, 2024, May 29-June 24, 2024, and August 22-September 06, 2024. Geological data are from Willsey and Günzler (2024) and IMO (2024). Coordinates are in decimal degrees using the WGS84 reference system.

6. Discussion

Efficient mapping of lava flow fields and monitoring volcanic activity are essential for hazard mitigation and for understanding the behavior of active volcanoes. Currently, various satellite sensors provide infrared thermal data at different spatial and temporal resolutions. The findings of this study confirm the capability of the Random Forest algorithm trained by Corradino et al. (2022) to detect thermal anomalies using spectral observations. Notably, the RF model demonstrated strong generalization, successfully mapping thermal anomalies from different eruptions near Grindavík. Thermal anomalies identified by the algorithm in GEE can be downloaded as typo-KML files, which are compatible with QGIS-type platforms. This enables near real-time tracking of lava flow development and the creation of geological maps that are continuously updated.

The case study application in Iceland – a geologically complex and challenging island – proved effective for detecting and accurately mapping lava flows. However, a few challenges and nuances were observed during the evaluations.

In certain cases, lava flow extents were overestimated due to factors such as refractive halos or cloud cover (Fig. 6a). These factors may interfere with the algorithm's ability to accurately distinguish active lava flow areas. Figure 8 illustrates the difference between the satellite image (Fig. 8a) and the thermal anomalies mapped directly onto the visible image (Fig. 8b). This example highlights the overestimation caused by halos in the satellite image. Therefore, it is critical to focus on the red-mapped areas and not the yellow ones, because they represent the hottest regions. Thus, a more accurate estimate is obtained that likely reflects the true extent of the lava flows. Conversely, slight underestimations were noted when the lava had already started cooling, as reduced heat emission from the cooling lava makes detection by thermal sensors more difficult (Figs. 4b and 7d). However, this information is of great relevance for detecting lava fields that are cooling and/or no longer active. For hazard mitigation, it is important to have information about the state of volcano activity and the progress of the lava flows.

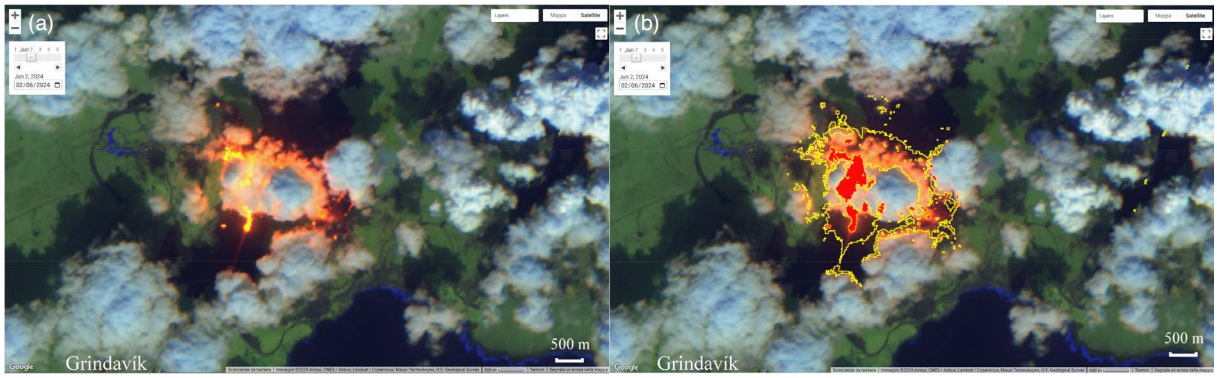

Figure 8. Difference between a) the satellite image, and b) the thermal anomalies mapped directly onto the visible image. The area mapped in red represents the hottest regions. All the images were captured via Google Earth Engine. The figure shows the contours of the anomaly in yellow and the hottest pixels within the segmented anomaly in red.

The algorithm by Corradino et al. (2022), when applied to monitoring the Sundhnúkur eruption, demonstrated its ability to accurately map thermal anomalies corresponding to the periods of highest volcanic activity, as shown in Fig. 9a. A total of 24 Sentinel-2 MSI images were analyzed. The algorithm performed well, even when applied to a volcano not included in the training phase. This is likely due to the Random Forest model being trained on large-scale eruptive events from diverse regions worldwide, enabling it to identify key characteristics for correctly classifying thermal anomalies, from cooler areas to the most intense, glowing regions, with a low rate of missed detections.

However, overestimation caused by halo effects preset in the yellow maps are reduced considering only red maps while underestimation in cases of cooling lava highlight the need to account for satellite sensors with thermal bands sensitive to lower thermal features and adaptation of monitoring strategies. Additionally, due to the unavailability of S2-MSI images between December 2023 and January 2024, and the persistent cloud cover in the region, it was not possible to map certain portions of the lava field. This limitation is evident when comparing the thermal anomaly

map (Fig. 9a) with the total areal coverage map from December 2023 to September 2024 (Fig. 9b). The algorithm of Corradino et al. (2022) proves highly effective in favorable meteorological conditions (see Fig. 4a), allowing near real-time monitoring of lava flow development and an excellent tool to use in conjunction with data obtained in the field. Notably, the areal extent of the lava field from the February 8-9, 2024 eruption was calculated, as it was fully identified by the algorithm. The analysis indicates an area of 3.38 km^2, compared with the actual 3.97 km^2 (Willsey and Günzler, 2024; IMO 2024). This confirms the algorithm's excellent ability to detect thermal anomalies associated with lava flows. Although, due to missing data and adverse weather conditions, the total lava field area for the entire Sundhnúkur eruption could not be estimated, from the thermal anomalies I calculated a lava flow area of 12.14 km^2, compared with the 38.02 km^2 estimated by Willsey and Günzler (2024) and IMO (2024).

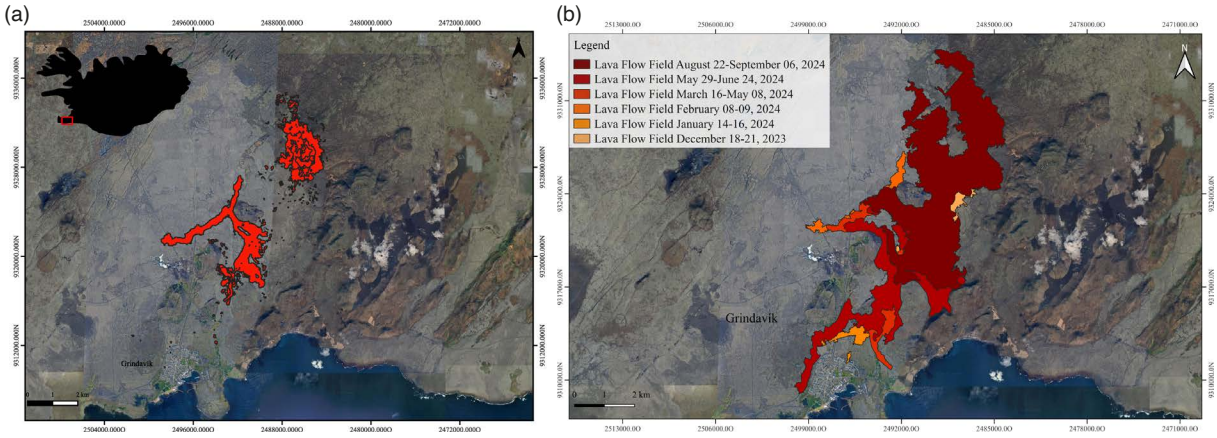

Figure 9. (a) Lava flows mapped from January to September 2024 during the Sundhnúkur eruption in the area near Grindavík identified using S2-MSI images and processed by the Random Forest algorithm in GEE (Corradino et al., 2022). The images downloaded from GEE in typo-KLM format were imported into QGIS (http://www.qgis.org); (b) Comparison with the actual areal of lava fields mapped by Willsey and Günzler (2024) and IMO (2024). Coordinates are in decimal degrees using the WGS84 reference system.

Additionally, this case study enabled the identification of a pre-eruptive thermal observation, particularly on August 19, 2024 (Fig. 7a), just a few days before the eruptive cycle that occurred from August 22 to September 6, 2024. While the most intense volcanic activity occurred further north, weaker activity was observed at the site of the thermal anomaly (Figs. 7b-c; IMO, 2024). In other instances, cloud cover in the days leading up to eruptions prevented similar observations. Observations of pre-eruptive thermal anomalies have already been verified by Corradino et al. (2024) at other volcanoes using the unsupervised Isolation Forest algorithm. Detection of pre-eruptive thermal anomalies from satellites using ML can therefore be used for near real-time monitoring, especially in areas with few or no ground-based monitoring systems.

7. Conclusions

This study demonstrates the effectiveness of the Random Forest algorithm (Corradino et al., 2022) in detecting thermal anomalies during the Sundhnúkur eruption, using high-resolution Sentinel-2 imagery. A key feature of this approach is its ability to visualize areas of heightened thermal activity in near real-time, with the hottest regions highlighted in red on the generated maps. These red areas correspond to zones with the highest temperatures, typically associated with active or recently erupted lava. This method of mapping is particularly valuable for tracking the temporal evolution of lava flows, allowing for precise monitoring of lava front propagation and eruption intensity, used in conjunction with other methods (e.g. UAVs, field surveys, etc.).

The detailed heat maps produced, which can be exported as typo-KML files and integrated into GIS platforms like QGIS, enable researchers and emergency managers to overlay thermal anomaly data on visible satellite imagery. This allows for a direct comparison between the heat distribution and the actual ground conditions. By focusing

on the red-colored regions – representing the hottest zones – the strategy provides a more accurate representation of active lava flow extents, minimizing overestimation caused by halos or reflections present in spectral images.

However, the study also identifies limitations of the RF model, i.e. overestimation of lava flows due to refractive halos when using yellow map and cloud cover, as well as limitations of only using S2-MSI data, i.e. underestimation in cases of cooling lava due to the absence of thermal bands sensitive to lower temperatures, which results in reduced thermal emissions detectable by sensors. A potential solution for persistent cloud cover could involve integrating SAR data. These challenges emphasize the need for continuous refinement of monitoring strategies and data fusion strategies. Despite these limitations, it was still possible to estimate the areal extent of the lava field from the February 8, 2024 eruption with high precision.

Furthermore, the inability to acquire satellite images during key periods – due to cloud cover or missed satellite passes – hindered the full mapping of lava flows. Nevertheless, the utility of these heat maps extends beyond tracking active eruptions. In certain cases, such as the detection of a pre-eruptive thermal observation on August 19, 2024, this method has proven beneficial. This capability is particularly valuable in regions with limited ground-based monitoring, where satellite observations can play a critical role in enhancing hazard prevention and response efforts.

Acknowledgements. This work was developed within the framework of the Laboratory of Technologies for Volcanology (TechnoLab) at the Istituto Nazionale di Geofisica e Vulcanologia (INGV) in Catania (Italy). This research was funded by the ATHOS Research Program (INGV OB.FU. 0867.010), by the 2019 Strategic Project FIRST – ForecastIng eRuptive activity at Stromboli volcano: timing, eruptive style, size, intensity, and duration – of the INGV Volcanoes Department (Delibera n. 144/2020), and by Project INGV Pianeta Dinamico VT_ORME 2023-2025 (INGV OB.FU. 1020.010). We are grateful to European Space Agency (ESA) for satellite data. Note: Google CoLaboratory™ is a trademark of Google LLC – ©2018 Google LLC All rights reserved.

References

Abrams, M., E. Abbott and A. Kahle (1991). Combined use of visible, reflected infrared, and thermal infrared images for mapping Hawaiian lava flows, J. Geophys. Res. Solid Earth, 96, B1, 475-484, doi:10.1029/90JB01392.

Albino, F., B. Smets, N. d'Oreye and F. Kervyn (2015). High-resolution TanDEM-X DEM: An accurate method to estimate lava flow volumes at Nyamulagira Volcano (DR Congo), J. Geophys. Res. Solid Earth, 120, 6, 4189-4207, doi:10.1002/2015JB011988.

Amato, E., C. Corradino, F. Torrisi and C. Del Negro (2021). Mapping lava flows at Etna Volcano using Google Earth Engine, open-access satellite data, and machine learning, in 2021 International Conference on Electrical, Computer, Communications and Mechatronics Engineering (ICECCME), IEEE, 1-6, doi:10.1109/ICECCME52200.2021.9591110.

Amato, E., C. Corradino, F. Torrisi and C. Del Negro (2023). A Deep convolutional neural network for detecting volcanic thermal anomalies from satellite images, Remote Sens., 15, 15, 3718, doi:10.3390/rs15153718.

Blackett, M. (2013). Review of the utility of infrared remote sensing for detecting and monitoring volcanic activity with the case study of shortwave infrared data for Lascar Volcano from 2001-2005, Geol. Soc. Spec. Publ., 380, 1, 107-135, doi:10.1144/SP380.10.

Bilotta, G., A. Cappello, A. Hérault and C. Del Negro (2019). Influence of topographic data uncertainties and model resolution on the numerical simulation of lava flows, Environ. Model. Softw., 112, 1-15, doi:10.1016/j.envsoft.2018.11.001.

Bindeman, I. N., F. M. Deegan, V. R. Troll, T. Thordarson et al. (2022). Diverse mantle components with invariant oxygen isotopes in the 2021 Fagradalsfjall eruption, Iceland, Nat. Commun., 13, 3737, doi:10.1038/s41467-022-31348-7.

Calabro, M. D., D. A. Schmidt and J. J. Roering (2010). An examination of seasonal deformation at the Portuguese Bend landslide, southern California, using radar interferometry, J. Geophys. Res. Earth Surf., 115, F2, doi:10.1029/2009JF001314.

Calder, E. S., R. Luckett, R. S. J. Sparks and B. Voight (2002). Mechanisms of lava dome instability and generation of rockfalls and pyroclastic flows at Soufrière Hills Volcano, Montserrat, Geol. Soc. Lond. Mem., 21, 1, 173-190, doi:10.1144/GSL.MEM.2002.021.01.08.

Calvari, S., M. Coltelli, M. Neri, M. Pompilio et al. (1994). The 1991-1993 Etna eruption: Chronology and lava, Acta Vulcanologica, 4, 1-14.

Caracciolo, A., E. Bali, E. Ranta, S. A. Halldórsson et al. (2024). Medieval and recent SO2 budgets in the Reykjanes Peninsula: Implication for future hazard, Geochem. Perspect. Lett., 30, 20-27, doi:10.7185/geochemlet.2417.

Cariello, S., C. Corradino, F. Torrisi and C. Del Negro (2023). Cascading machine learning to monitor volcanic thermal activity using orbital infrared data: From detection to quantitative evaluation, Remote Sens., 16, 1, 171, doi:10.3390/rs16010171.

Carracedo, J. C., V. R. Troll, J. M. Day, H. Geiger et al. (2022). The 2021 eruption of the Cumbre Vieja volcanic ridge on La Palma, Canary Islands, Geol. Today, 38, 3, 94-107, doi:10.1111/gto.12388.

Cas, R., J. V. Wright and G. Giordano (2024). Basaltic and Other Low-Viscosity Lavas: Eruption, Flow Behavior, and Features of Subaerial and Subaqueous Lavas, in Volcanology: Processes, Deposits, Geology and Resources, Springer International Publishing, Cham, 229-309, doi:10.1007/978-3-319-66613-6_5.

Corradino, C., G. Ganci, A. Cappello, G. Bilotta et al. (2019). Mapping recent lava flows at Mount Etna using multispectral Sentinel-2 images and machine learning techniques, Remote Sens., 11, 16, 1916, doi:10.3390/rs11161916.

Corradino, C., E. Amato, F. Torrisi and C. Del Negro (2022). Data-driven random forest models for detecting volcanic hot spots in Sentinel-2 MSI images, Remote Sens., 14, 17, 4370, doi:10.3390/rs14174370.

Corradino, C., A. B. Malaguti, M. S. Ramsey and C. Del Negro (2024). Quantitative Assessment of Volcanic Thermal Activity from Space Using an Isolation Forest Machine Learning Algorithm, Remote Sens., 16, 11, 2001, doi:10.3390/rs16112001.

Del Negro, C., A. Cappello and G. Ganci (2016). Quantifying lava flow hazards in response to effusive eruption, Geol. Soc. Am. Bull., 128, 5-6, 752-763, doi:10.1130/B31364.1.

Dietterich, H. R., M. P. Poland, D. A. Schmidt, K. V. Cashman et al. (2012). Tracking lava flow emplacement on the east rift zone of Kīlauea, Hawai ʻi, with synthetic aperture radar coherence, Geochem. Geophys. Geosyst., 13, 5, doi:10.1029/2011GC004016.

Diniega, S., S. E. Smrekar, S. Anderson and E. R. Stofan (2013). The influence of temperature-dependent viscosity on lava flow dynamics, J. Geophys. Res. Earth Surf., 118, 3, 1516-1532, doi:10.1002/jgrf.20111.

Einarsson, P. (2008). Plate boundaries, rifts and transforms in Iceland, Jökull, 58, 12, 35-58, doi:10.33799/jokull2008.58.035.

EO Browser, Planet Labs company, https://apps.sentinel-hub.com/eo-browser/, Sinergise Solutions d.o.o.

Ferrentino, E., C. Bignami, F. Nunziata, S. Stramondo et al. (2023). On the ability of dual-polarimetric SAR measurements to observe lava flows under different volcanic environments, Int. J. Appl. Earth Obs. Geoinf., 123, 103471, doi:10.1016/j.jag.2023.103471.

Frazzetta, G. and R. Romano (1984). The 1983 Etna eruption: event chronology and morphological evolution of the lava flow, Bull. Volcanol., 47, 1079-1096, doi:10.1007/BF01952364.

Ganci, G., A. Cappello, V. Zago, G. Bilotta et al. (2019). 3D Lava flow mapping of the 17-25 May 2016 Etna eruption using tri-stereo optical satellite data, Ann. Geophys., 62, 2, VO220, doi:10.4401/ag-7875.

Genzano, N., N. Pergola and F. Marchese (2020). A Google Earth Engine tool to investigate, map and monitor volcanic thermal anomalies at global scale by means of mid-high spatial resolution satellite data, Remote Sens., 12, 19, 3232, doi:10.3390/rs12193232.

Ghimire, B., J. Rogan, V. R. Galiano, P. Panday et al. (2012). An evaluation of bagging, boosting, and random forests for land-cover classification in Cape Cod, Massachusetts, USA, GISci. Remote Sens., 49, 5, 623-643, doi:10.2747/1548-1603.49.5.623.

Gregg, T. K. (2017). Patterns and processes: Subaerial lava flow morphologies: A review, J. Volcanol. Geotherm. Res., 342, 3-12, doi:10.1016/j.jvolgeores.2017.04.022.

Griffiths, R. W. (2000). The dynamics of lava flows. Annual review of fluid mechanics, 32, 1, 477-518, doi:10.1146/annurev.fluid.32.1.477.

Gorelick, N., M. Hancher, M. Dixon, S. Ilyushchenko et al. (2017). Google Earth Engine: Planetary-scale geospatial analysis for everyone, Remote Sens. Environ., 202, 18-27, doi:10.1016/j.rse.2017.06.031.

Gudmundsson, M. T., T. Thordarson, A. Höskuldsson, G. Larsen et al. (2012). Ash generation and distribution from the April-May 2010 eruption of Eyjafjallajökull, Iceland, Sci. Rep., 2, 1, 572, doi:10.1038/srep00572.

Harris, A. (2013). Thermal remote sensing of active volcanoes: a user's manual, Cambridge University Press, 728, doi:10.1017/CBO9781139029346.

Hastie, T., R. Tibshirani, J. Friedman, T. Hastie et al. (2009). Random forests, in The elements of statistical learning: Data mining, inference, and prediction, Springer Series in Statistics, New York, 587-604, doi:10.1007/b94608.

Hird, J. N., E. R. DeLancey, G. J. McDermid and J. Kariyeva (2017). Google Earth Engine, open-access satellite data, and machine learning in support of large-area probabilistic wetland mapping, Remote Sens., 9, 12, 1315, doi:10.3390/rs9121315.

Horiuchi, S. S. and H. Iwamori (2016). A consistent model for fluid distribution, viscosity distribution, and flow-thermal structure in subduction zone, J. Geophys. Res. Solid Earth, 121, 5, 3238-3260, doi:10.1002/2015JB012384.

Icelandic Meteorological Office, IMO (2024). https://en.vedur.is/about-imo/news/volcanic-unrest-grindavik.

Kervyn, M., F. Kervyn, R. Goossens, S. K. Rowland et al. (2007). Mapping volcanic terrain using high-resolution and 3D satellite remote sensing, Geol. Soc. Spec. Publ., 283, 1, 5-30, doi:10.1144/SP283.2.

Kubanek, J., J. A. Richardson, S. J. Charbonnier and L. J. Connor, (2015). Lava flow mapping and volume calculations for the 2012-2013 Tolbachik, Kamchatka, fissure eruption using bistatic TanDEM-X InSAR, Bull. Volcanol., 77, 1-13, doi:10.1007/s00445-015-0989-9.

Lu, Z., R. Rykhus, T. Masterlark and K. G. Dean (2004). Mapping recent lava flows at Westdahl Volcano, Alaska, using radar and optical satellite imagery, Remote Sens. Environ., 91, 3-4, 345-353, doi:10.1016/j.rse.2004.03.015.

Manea, V. and M. Gurnis (2007). Subduction zone evolution and low viscosity wedges and channels, Earth Planet. Sci. Lett., 264, 1-2, 22-45, doi:10.1016/j.epsl.2007.08.030.

Marchese, F., N. Genzano, M. Neri, A. Falconieri et al. (2019). A multi-channel algorithm for mapping volcanic thermal anomalies by means of Sentinel-2 MSI and Landsat-8 OLI data, Remote Sens., 11, 23, 2876, doi:10.3390/rs11232876.

Marchese, F., C. Filizzola, T. Lacava, A. Falconieri et al. (2021). Mt. Etna paroxysms of February-April 2021 monitored and quantified through a multi-platform satellite observing system, Remote Sens., 13, 16, 3074, doi:10.3390/rs13163074.

Saemundsson, K. and M. Sigurgeirsson (2013). Reykjanesskagi, in Náttúruvá á Íslandi – Eldgos og jarðskjálftar Sólnes, Sigmundsson and Bessason (Eds.), University of Iceland Press, 379-401.

Sæmundsson, K., H. Jóhannesson, A. Hjartarson, S. G. Kristinsson et al. (2016). Geological Map of Southwest Iceland, 1:100000, Iceland Geosurvey.

Saemundsson, K., M. Sigurgeirsson and G. Ó. Fridleifsson (2020). Geology and structure of the Reykjanes volcanic system, Iceland, J. Volcanol. Geothermal. Res., 391, 106501, doi:10.1016/j.jvolgeores.2018.11.022.

Servadio, Z., N. Villeneuve and P. Bachlery (2012). Automatic mapping of the lava flows at Piton de la Fournaise volcano, by combining thermal data in near and visible infrared, in Remote Sensing-Applications B. Escalante Ramirez (Ed.), InTech, Rijeka, Croatia, 201-220, doi:10.5772/37685.

Soule, S. A. (2015). Mid-ocean ridge volcanism, in The encyclopedia of volcanoes, Academic Press, 395-403, doi:10.1016/B978-0-12-385938-9.00021-3.

Spampinato, L., S. Calvari, C. Oppenheimer and E. Boschi (2011). Volcano surveillance using infrared cameras, Earth Sci. Rev., 106, 1-2, 63-91, doi:10.1016/j.earscirev.2011.01.003.

Spinetti, C., F. Mazzarini, R. Casacchia, L. Colini et al. (2009). Spectral properties of volcanic materials from hyperspectral field and satellite data compared with LiDAR data at Mt. Etna, Int. J. Appl. Earth Obs. Geoinf., 11, 2, 142-155, doi:10.1016/j.jag.2009.01.001.

Torrisi, F., C. Corradino, S. Cariello and C. Del Negro (2024). Enhancing detection of volcanic ash clouds from space with convolutional neural networks, J. Volcanol. Geotherm. Res., 448, 108046, doi:10.1016/j.jvolgeores.2024.108046.

Wadge, G., B. Scheuchl and N. F. Stevens (2002). Spaceborne radar measurements of the eruption of Soufrière Hills Volcano, Montserrat, Geol. Soc. Lond. Mem., 21, 1, 583-594, doi:0.1144/GSL.MEM.2002.021.01.27.

Willsey, S. and D. Günzler (2024). Svartsengi Lava Flow Map, https://kleinergeologe.github.io/Iceland-map/#12/63.8901/-22.3870.

Wolfe, C. J., I. T. Bjarnason, J. C. VanDecar and S. C. Solomon (1997). Seismic structure of the Iceland mantle plume, Nature, 385, 6613, 245-247, doi:10.1038/385245a0.

***CORRESPONDING AUTHOR: Arianna BEATRICE MALAGUTI**,
Istituto Nazionale di Geofisica e Vulcanologia, Sezione di Catania, Osservatorio Etneo, Catania, Italy
e-mail: arianna.malaguti@ingv.it